*metals*

MDPI

*Article*

# Correlation between Laser-Ultrasound and Microstructural Properties of Laser Melting Deposited Ti6Al4V/$B_4C$ Composites

**Wanwei Xu [1], Xue Bai [1,*], Zhonggang Sun [2], Xin Meng [2] and Zhongming Guo [1]**

[1] Laser Institute, Qilu University of Technology (Shandong Academy of Sciences), Jinan 250103, China; xuwanwei0520@163.com (W.X.); zgsdgzm@163.com (Z.G.)
[2] Tech Institute for Advanced Materials, College of Materials Science and Technology, Nanjing Tech University, Nanjing 210009, China; sunzgg@njtech.edu.cn (Z.S.); 202121014@mail.sdu.edu.cn (X.M.)
* Correspondence: baix@sdlaser.cn

**Abstract:** The presence of large microtextured clusters (MTC) composed of small α-phase crystallites with preferred crystallographic orientations in 3D printed near-α titanium alloys leads to poor mechanical and fatigue properties. It is therefore crucial to characterize the size of MTCs nondestructively. Ti6Al4V/$B_4C$ composite materials are manufactured using Laser Melting Deposition (LMD) technology by adding an amount of nano-sized $B_4C$ particles to the original Ti6Al4V powder. TiB and TiC reinforcements precipitating at grain boundaries stimulate the elongated α crystallites and coarse columnar MTCs to equiaxed transition, and microstructures composed of approximately equiaxed MTCs with different mean sizes of 11–50 μm are obtained. Theoretical models for scattering-induced attenuation and centroid frequency downshift of ultrasonic waves propagating in such a polycrystalline medium are presented. It is indicated that, the studied composite material has an extremely narrow crystallographic orientation distribution width, i.e., a strong degree of anisotropy in MTCs. Therefore, MTCs make a dominant contribution to the total scattering-induced attenuation and spectral centroid frequency downshift, while the contribution of fine α-phase crystallites is insignificant. Laser ultrasonic inspection is performed, and the correlation between laser-generated ultrasonic wave properties and microstructural properties of the Ti6Al4V/$B_4C$ composites is analyzed. Results have shown that the deviation between the experimentally measured ultrasonic velocity and the theoretical result determined by the Voigt-averaged velocity in each crystallite is no more than 2.23%, which is in good agreement with the degree of macroscopically anisotropy in the composite specimens. The ultrasonic velocity seems to be insensitive to the size of MTCs, while the spectral centroid frequency downshift is approximately linear to the mean size of MTCs with a goodness-of-fit ($R^2$) up to 0.99. Actually, for a macroscopically untextured near-α titanium alloy with a relatively narrow crystallographic orientation distribution, the ultrasonic velocity is not correlated with the properties of MTCs, by contrast, the central frequency downshift is dominated by the size and morphology of MTCs, showing great potentials in grain size evaluation.

**Keywords:** laser-ultrasonics; laser melting deposition; metal composites; ultrasonic scattering; centroid frequency shift

check for updates

**Citation:** Xu, W.; Bai, X.; Sun, Z.; Meng, X.; Guo, Z. Correlation between Laser-Ultrasound and Microstructural Properties of Laser Melting Deposited Ti6Al4V/$B_4C$ Composites. *Metals* **2021**, *11*, 1951. https://doi.org/10.3390/met11121951

Academic Editor: Zhiwei Liu

Received: 28 October 2021
Accepted: 30 November 2021
Published: 3 December 2021

**Publisher's Note:** MDPI stays neutral with regard to jurisdictional claims in published maps and institutional affiliations.

**Copyright:** © 2021 by the authors. Licensee MDPI, Basel, Switzerland. This article is an open access article distributed under the terms and conditions of the Creative Commons Attribution (CC BY) license (https://creativecommons.org/licenses/by/4.0/).

## 1. Introduction

Metal 3D printing technology, as an additive manufacturing technology, has the advantages of high deposition efficiency, low manufacturing cost, and a high degree of design freedom, lightweight design and functional integration over the conventional formative or subtractive manufacturing [1–4]. It shows broad prospects for technological industrialization in the fields of medical, automotive, nuclear power, and aerospace [4,5]. Laser Melting Deposition (LMD) technology, as one of the metal 3D printing technologies, has attracted researchers' attention. Based on different forms of raw materials, there are two LMD forming processes: powder feed and wire feed, which have different advantages and

applications. The LMD with powder feed gives better resolution and surface finish and it has the advantages of high matrix bonding strength, and uniform and dense microstructure. While the LMD with wire feed is considered to be a promising method for forming large components owing to its high deposition rate, high material utilization rate, and relatively low costs of manufacturing and equipment [6–10]. During the LMD forming process, the sample will experience transient heating and melting at a point heat source followed by rapid cooling, resulting in a large temperature gradient between the melt pool and the substrate. For near-$\alpha$ titanium alloys, which are widely used in aircraft engine, the large temperature gradient can lead to the appearance of large microtextured clusters (MTC) running through several cladding layers, which are composed of fine $\alpha$-phase crystallites with preferred crystallographic orientations [11,12]. Studies have shown that the presence of large MTCs can result in poor performance and significant anisotropy of the components, and even lead to early failure due to dwell fatigue [13–15]. Since the large MTCs have remarkable effects on the mechanical and fatigue properties, it is crucial to evaluate the mean size of MTCs for optimizing the mechanical and fatigue properties of laser melting deposited components [16,17]. LMD is considered as a one-step direct forming technology, the destructive methods for grain size evaluation, such as optical metallography and electron backscatter diffraction (EBSD), can no longer meet the detection requirement, and thus the non-destructive evaluation of microstructural properties is particularly important. Among many non-destructive testing technologies, the ultrasonic testing technology has shown great potentials due to its high sensitivity, strong penetrability, and wide applicability for materials. In particular, laser ultrasonic technology has the capability of non-contact and on-line real-time inspection at high temperatures or on moving surfaces. It shows great potentials in both off-line and on-line characterization of material microstructures.

When an ultrasonic wave propagates through polycrystalline materials, the elastic properties and density inhomogeneity of individual crystallites result in the variation of velocities of ultrasonic waves in each crystallite, causing scattering of ultrasonic waves at grain boundaries and resulting in the variation of ultrasonic propagation properties, such as the propagation velocity, the amplitude attenuation and the scattered noises. It is believed that information on microstructure features, such as grain size, crystallographic and morphological textures, can be obtained by inversion of ultrasonic wave properties. Correlation of ultrasonic wave properties to microstructural features is a fundamental research for the non-destructive evaluation of microstructural evolution.

Ultrasonic velocity is often used to evaluate the mean grain size since its measurement is relatively simple and straightforward. Hirsekorn et al. [18,19] proposed a theoretical model for planar ultrasonic longitudinal and transverse wave velocities as a function of grain size in polycrystalline materials. Ünal et al. [20] measured ultrasonic wave velocity in boron carbide ($B_4C$)-aluminium (Al) and $B_4C$-nickel (Ni) composites using a piezoelectric ultrasonic transducer and found an approximately linear relationship between the ultrasonic velocity and the grain size. However, studies have shown that this method has less sensitivity to some metal materials, causing a relatively large error of grain size evaluation [21].

Recently, more and more researchers focus on the spectral analysis, and use the ultrasonic features, such as the attenuation and the backscattered noises, to evaluate grain size of polycrystalline materials. Özkan et al. [22] compared ultrasonic velocity, ultrasonic attenuation, the rate of peak heights for grain size characterization of $B_4C$-Al composite materials. Results showed a higher correlation between ultrasonic attenuation and grain size variation. Furthermore, theoretical studies [23,24] have showed that ultrasonic attenuation has an exponential relationship with grain size, and a large number of experiments [25–30] have been performed for grain size characterization by inversion of ultrasonic attenuation in both weakly [25] and strongly [26–30] scattering materials. Nevertheless, the research on ultrasonic attenuation is usually restricted by signal-to-noise ratio (SNR) for strongly scattering materials. Thus, research efforts have also been dedicated to backscattered

noise signals. Theoretical models for ultrasonic backscattering coefficient in both single-phase [31] and duplex [32] microstructures have been proposed based on the isolated scatterer model, i.e., the single-scattering assumption, and effects of grain size and grain shape on ultrasonic backscattering have been investigated [15,33]. However, the aforementioned methods are still amplitude-based approaches. Since the amplitude measurement accuracy of ultrasonic signals is closely related to the stability of the ultrasonic inspection system, it can largely affect the accuracy of grain size evaluation [34]. Besides, the accuracy of the ultrasonic attenuation method is also influenced by the attenuation sources from absorption, geometric spreading and dislocation in materials [35]. The backscattering coefficient tends to be stable with the increase of grain size at a given frequency, so the range of grain sizes evaluated by the backscattering method is relatively narrow [33,36].

In view of the limitations of the aforementioned methods, emphasis has been placed on research about grain size effects on ultrasonic centroid frequency shift. Studies have showed that high-frequency components of ultrasonic signals experience greater attenuation than low-frequency components, which results in a downshift in the centroid frequency of the ultrasonic pulse echo [37]. Moreover, the centroid frequency downshift is more significant as the grain size increases. The centroid frequency shift method is insensitive to the geometric spreading, wave reflection and transmission effects, and can effectively avoid the error caused by the instability of laser-ultrasonic signal amplitude measurement. Thus this method can evaluate the grain size more accurately [38,39].

There have been some advances in ultrasonic characterization for grain size of 3D printed metals or composites by use of the above-mentioned methods. Traditional ultrasonic techniques are first used since the detection signals have a good SNR. Yang et al. [40] found that the longitudinal wave velocity along the deposition direction was about 2% lower than the velocity perpendicular to the deposition direction using immersion ultrasonic testing method, thus verifying the anisotropy of additively manufactured TC18. Laser ultrasonics, as a new technology capable of online real-time non-contact detection at high temperatures, has been demonstrated to be promising for inspection of internal defects of additively manufactured components [41,42]. Nevertheless, research on its application to the microstructure characterization is still insufficient. Ma et al. [43] evaluated the grain size of 3D printed titanium alloy using laser ultrasonic technology, and results showed that the ultrasonic attenuation exhibited a linear relationship with the mean grain size, but the applicable range of material and frequency of this linear relationship model still need to be confirmed by theoretical derivation and extensive experimental studies. In this paper, the laser ultrasonic technology is used for detecting Ti6Al4V/$B_4C$ composite specimens manufactured by the LMD of powder feed. Theoretical models for scattering-induced attenuation and centroid frequency downshift of ultrasonic waves propagating in the studied composite materials are presented. Effects of microstructural properties on laser-generated ultrasonic wave characteristics, such as the ultrasonic velocity and the spectral centroid frequency shift of ultrasonic echoes are analyzed. This would lay a research foundation for the non-destructive evaluation of grain size in 3D printed metal composite materials.

This paper proceeds as follows: Section 2 is devoted to methods for sample preparation and ultrasonic experiment. In Section 3, theoretical models for scattering-induced attenuation and centroid frequency downshift of ultrasonic waves are presented. Then, the correlation of laser-ultrasound to microstructural properties of laser melting deposited Ti6Al4V/$B_4C$ composites is described in Section 4. Finally, main conclusions are summarized in Section 5.

## 2. Materials and Methods

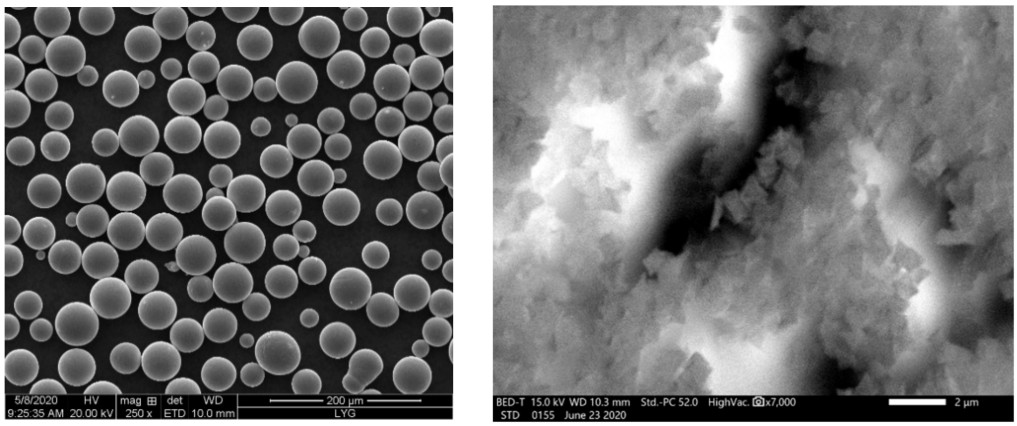
### *2.1. Materials*

Ti6Al4V alloys have been widely used because of high melting point, high melt state activity and high deformation resistance [44,45]. In this paper, four Ti6Al4V/$B_4C$ composite specimens of $30 \times 30 \times 10$ mm$^3$ were prepared using LMD by adding an amount of $B_4C$ particles to the gas atomized Ti6Al4V alloy spherical powder [46]. Following the

principle of single factor experiment design, the mass percentages of $B_4C$ particles in the four specimens were 0%, 1%, 3%, 5%, and the corresponding specimens were denoted as Ti6Al4V, TMC1, TMC2, TMC3, respectively. The two powders were mixed in a two-conical mixer (ZX-0.01 $m^3$), tumbled at 25 RPM for 6 h to improve the fluidity, and then dried in vacuum for 4 h [46]. The chemical composition and the mixture proportions of the two powders are listed in Table 1. The morphologies of Ti6Al4V alloy spherical powder and $B_4C$ powder obtained by scanning electron microscope (SEM) technology (Zeiss Inc., Oberkochen, Germany) are shown in Figure 1. The $B_4C$ powder is nano-sized and the averaged size is about 50 nm. The granulometric analysis of the Ti6Al4V powder determined by Microtrac Sync laser particle size analyzer (Microtrac Inc., Montgomeryville, PA, USA) is displayed in Figure 2. It is revealed that 95% of Ti6Al4V powder particles are in the size range of 80–200 µm. The particle size distribution function has a Gaussian shape with a goodness-of-fit ($R^2$) of 0.95, and the standard deviation is around 16 µm. The appropriate processing parameters were chosen for achieving good forming quality and minimum defects by using the single-track experiment method and the orthogonal experiment design, which are shown in Table 2 [46].

**Table 1.** Chemical composition and mixture proportions of Ti6Al4V and $B_4C$ powders [46].

| | Chemical Composition (wt. %) | | | | | | | | | Mixture Proportions (wt. %) | | | |
|---|---|---|---|---|---|---|---|---|---|---|---|---|---|
| | | | | | | | | | | Ti6Al4V | TMC1 | TMC2 | TMC3 |
| Ti6Al4V | Fe<br>0.15 | C<br>0.06 | Al<br>6.02 | V<br>4 | H<br>0.009 | N<br>0.03 | Si<br>0.04 | O<br>0.16 | Ti<br>Bal. | 100 | 99 | 97 | 95 |
| $B_4C$ | | O<br>0.04 | Mn<br>0.002 | F.C<br>0.04 | Ca<br>0.001 | Mg<br>0.001 | Fe<br>0.02 | $B_4C$<br>Bal. | | 0 | 1 | 3 | 5 |




(**a**) (**b**)

**Figure 1.** Morphologies of the Ti6Al4V alloy spherical powder and nano-sized $B_4C$ powder. (**a**) Ti6Al4V alloy powder; (**b**) $B_4C$ powder.

**Table 2.** Processing parameters of laser melting deposited Ti6Al4V/$B_4C$ composites.

| Processing Parameters | |
|---|---|
| Laser power | 1500 W |
| Laser scanning speed | 10 m/s |
| Powder feed rate | 6 g/min |
| Overlap ratio | 50% |

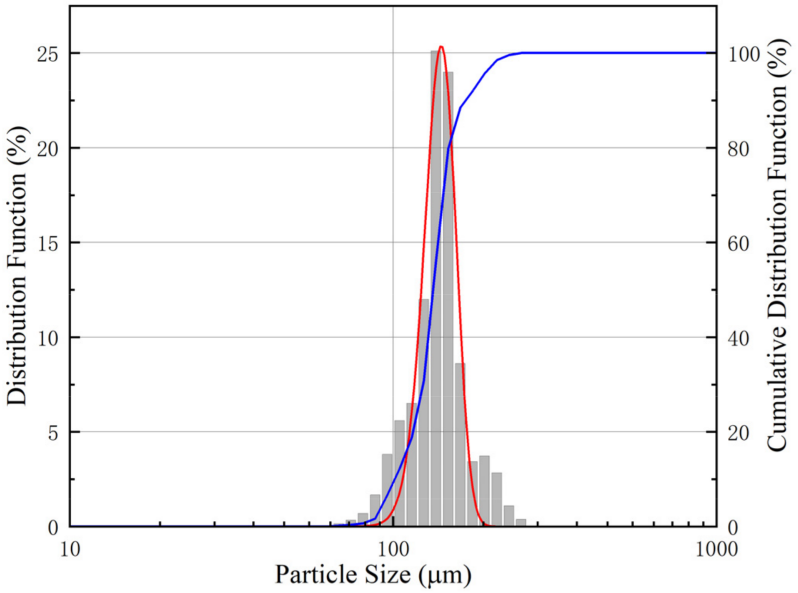


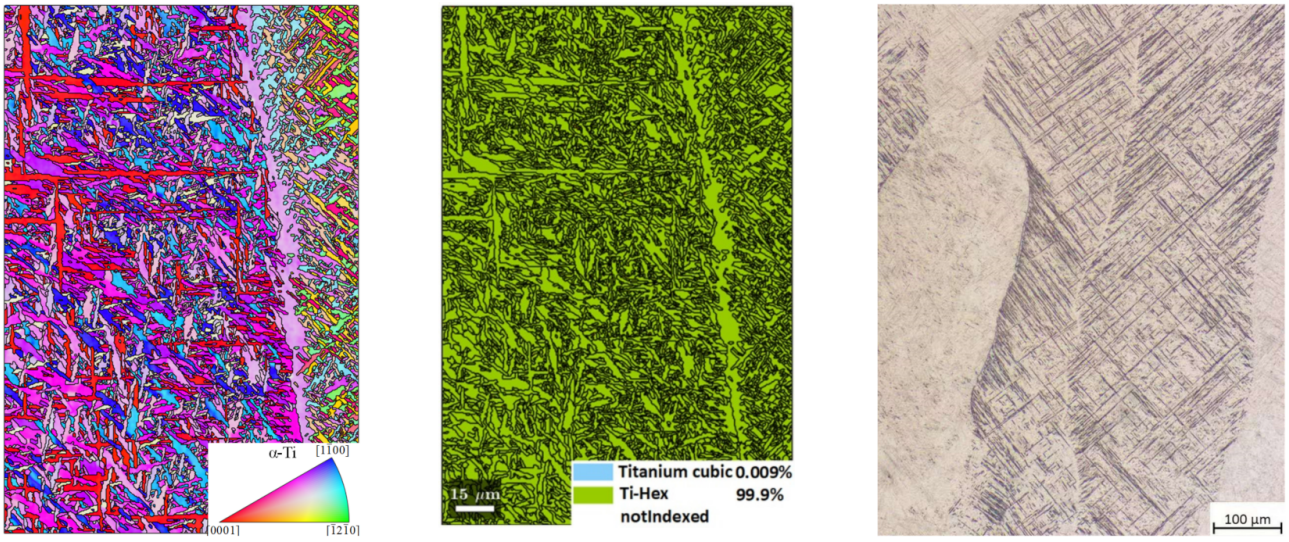

**Figure 2.** Particle size distribution of the Ti6Al4V alloy spherical powder presented as grey histograms. The fitted curve for Gaussian distribution is superposed in red solid line and the volume weighted cumulative distribution function is displayed in blue solid line.

EBSD and metallographic observations were performed to obtain the microstructural information. Specimens were cut along the smallest dimension direction, i.e., the direction of ultrasonic wave propagation, and then the cut surfaces were grinded, electrolytic polished, and finally etched. The EBSD orientation maps of the specimens were obtained via the orientation imaging microscopy (OIM) technique (TSL(EDAX), Mahwah, NJ, USA).

It is seen from the EBSD and metallographic observations in Figure 3 that the Ti6Al4V specimen is a near-α phase titanium alloy. Due to the temperature gradient among cladding layers during the forming process, the grains of laser melting deposited Ti6Al4V alloys grow in the normal direction to the substrate, forming MTCs composed of fine elongated hexagonal α-phase crystallites with preferred crystallographic orientations. The grain boundaries of MTCs are bright and continuous, and α-phase crystallites mainly grow along the direction of <0 0 0 1> in each MTC, leading to an elongated morphology with a large aspect ratio of 14. The mean grain size $\overline{D}$ is calculated by the mean equivalent area diameter, $\overline{D} = (4\overline{A}/\pi)^{0.5}$, where $\overline{A}$ is the arithmetic average of the grain areas. The mean sizes of α crystallites and MTCs are 1.8 and 400 μm, respectively.

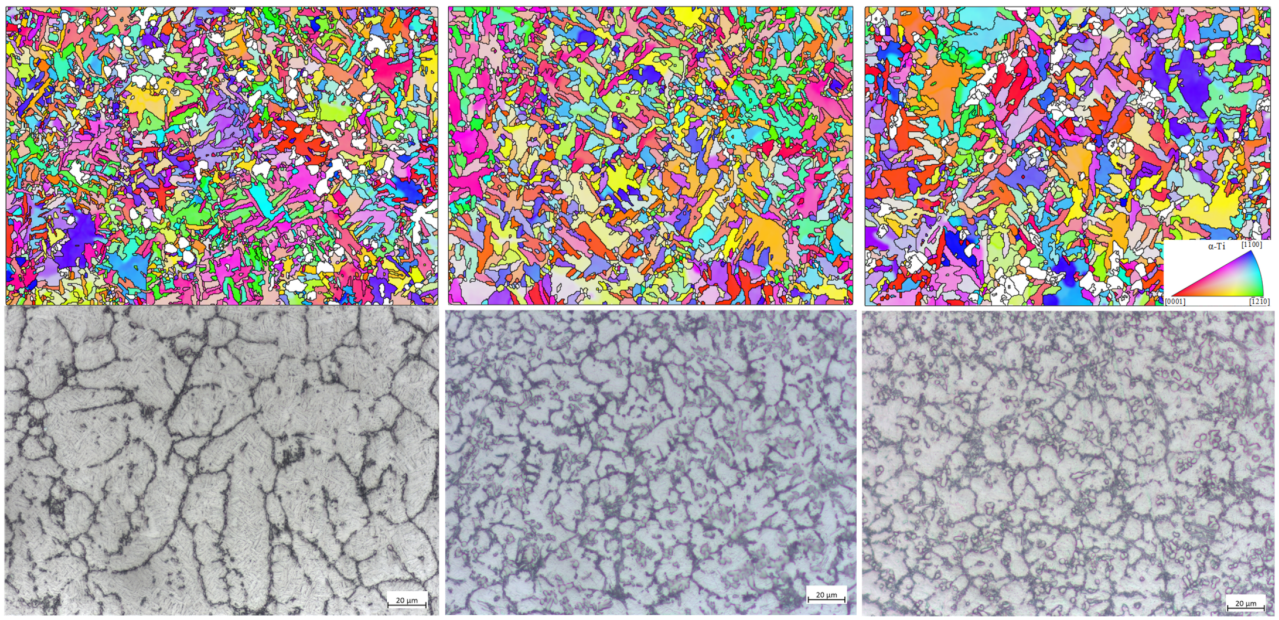
The EBSD and metallographic observations of TMC1, TMC2 and TMC3 are given in Figure 4. Compared with Ti6Al4V, the grain boundaries of MTCs are indistinguishable. This may be attributed to the decrease of anisotropy degree in each MTC. Besides, the aspect ratios of α crystallites are 3.8, 3.3 and 2.9 in TMC1, TMC2 and TMC3 specimens, respectively, which are much smaller than the one in Ti6Al4V specimen. It is suggested that the addition of nano-sized $B_4C$ particles stimulates the elongated α crystallites and coarse columnar MTCs to equiaxed transition. Actually, the in-situ reaction between Ti6Al4V and $B_4C$ promotes the generation of TiB and TiC reinforcements. These reinforcements precipitate at grain boundaries to restrict grain growth, and act as nucleation points to accelerate the nonspontaneous nucleation of MTCs for achieving fine grain strengthening [46]. The mean sizes of α crystallites in TMC1, TMC2 and TMC3 specimens are 1.8, 2.1 and 2.2 μm, respectively, and the mean sizes of MTCs are 50, 15 and 11 μm. It is indicated that the addition of $B_4C$ particles makes no big difference to the size of fine α crystallites, but can refine the size of coarse MTCs remarkably. It is seen from the phase diagrams of specimens (Figure 5) that all the Ti6Al4V/$B_4C$ composite specimens are near α-phase titanium alloys with the weight percentages of the reinforcement phases TiB and TiC no more than 6.61%

and 1.87%, respectively. Therefore, these reinforcement phases can be assumed to make a negligible contribution to the scattering-induced attenuation and centroid frequency shift.



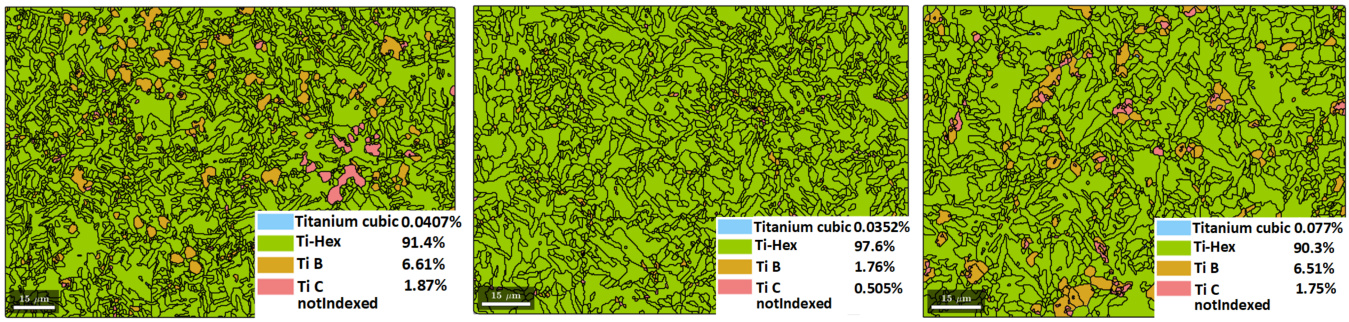

(**a**) (**b**) (**c**)

**Figure 3.** EBSD inverse pole figure (IPF) α orientation map and metallographic image taken along the deposition direction of laser melting deposited Ti6Al4V. (**a**) EBSD IPF α orientation map; (**b**) color coded map of Ti phases; (**c**) metallographic image.



(**a**) (**b**) (**c**)

**Figure 4.** EBSD IPF α orientation maps (the color images) and metallographic images (the black-and-white images) taken along the deposition direction of laser melting deposited Ti6Al4V/$B_4C$ composite specimens. (**a**) TMC1; (**b**) TMC2; (**c**) TMC3.




(**a**) (**b**) (**c**)

**Figure 5.** Phase diagrams of laser melting deposited Ti6Al4V/$B_4C$ composite specimens. (**a**) TMC1; (**b**) TMC2; (**c**) TMC3.

Based on the metallographic and EBSD observations discussed above, the studied Ti6Al4V/$B_4C$ composite specimens can be considered as near α-phase titanium alloys composed of larger equiaxed MTCs which consist of much smaller α crystallites with preferred orientations. It is revealed from the pole figures of $\{0001\}$, $\{10\bar{1}0\}$ and $\{2\bar{1}\bar{1}0\}$ planes for α crystallites (Figure 6) that the anisotropy of the material is relatively weak, indicating that the preferred crystallographic orientations in different MTCs can be assumed to be randomly oriented. This assumption would be an essential prerequisite for the theoretical derivation of ultrasonic scattering-induced attenuation in the Section 3.

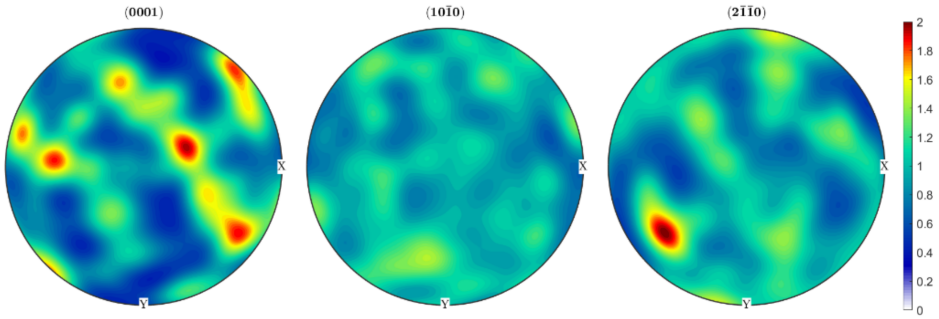



**Figure 6.** Pole figures of $\{0001\}$, $\{10\bar{1}0\}$, and $\{2\bar{1}\bar{1}0\}$ planes for α crystallites.

### *2.2. Experimental Setup*

Specimens were detected by use of the laser ultrasonic inspection system as shown in Figure 7. A Q-switched Nd:YAG pulsed laser (supplied by Quantel, Inc., Les Ulis, France) was used to excite the ultrasound on one side of the specimens, with laser pulse width of 8 ns. The spot diameter was 0.7 mm and the single pulse energy was approximately 25 mJ. Then, the ultrasonic transmission pulses were detected by the IOS AIR-1550-TWM laser ultrasonic receiver (supplied by Intelligent Optical Systems, Inc., Torrance, CA, USA) at the opposite surface of specimen. The pulsed laser can generate simultaneously a variety of modes of ultrasonic waves, such as longitudinal waves, transverse waves, and Rayleigh waves, etc. In the experimental system, the generation and detection of ultrasonic signals were set to be co-linearly aligned, so that only longitudinal waves were detected. The specimen was fixed on a two-dimensional scanning platform, so that multiple points on the detection surface of each specimen were detected to reduce the random error by using repeated measurement experimental design. The ultrasonic signal received by the laser ultrasonic receiver was passed to a digital oscilloscope for display and storage after being averaged 128 times, and was then processed to obtain the ultrasonic velocity and the spectral centroid frequency.

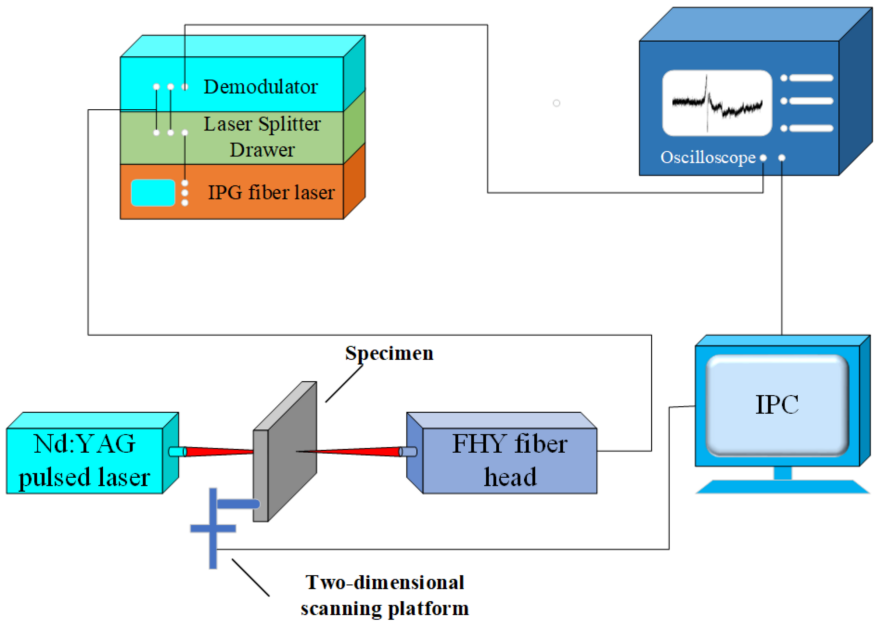



**Figure 7.** Schematic diagram of the laser-ultrasonic experimental inspection system.

## 3. Theoretical Models

In this section, the ultrasonic wave scattering mechanism at grain boundaries in the studied composite material is discussed, and the theoretical models for the scattering-induced attenuation and the spectral centroid frequency downshift are given.

### *3.1. Scattering-Induced Attenuation*

Here, two important assumptions are made for the theoretical derivation of the scattering-induced attenuation. Firstly, it is suggested from Figure 6 that the medium can be assumed to be macroscopically untextured and homogeneous. Secondly, it is seen from Figure 4 that there is a great difference in the length scale between coarse MTCs and fine $\alpha$ crystallites. It is thus believed that ultrasonic wave scattering by MTCs and by $\alpha$ crystallites are independent. On these assumptions, the scattering-induced attenuation can be determined by the sum of two independent components: the attenuation contributed by the fine $\alpha$ crystallites, $\alpha^{crystallities}$, and by the coarse MTCs, $\alpha^{MTC}$ [15]:

$$\alpha^{total} = \alpha^{crystallies} + \alpha^{MTC}, \tag{1}$$

where, the superscripts '*crystallites*' and '*MTC*' denote the fields associated with fine $\alpha$ crystallites and coarse MTCs, respectively.

The attenuation contributed by the fine $\alpha$ crystallites, $\alpha^{crystallites}$, is closely related to the orientation distribution function (ODF) of $\alpha$ crystallites, and can be calculated by the attenuation in a macroscopically isotropic and homogeneous $\alpha$-phase polycrystalline titanium, $\alpha^{\alpha Ti}$, multiplied by an ODF factor $M(\sigma)$ [15]:

$$\alpha^{crystallies} = M(\sigma)\alpha^{\alpha Ti}, \tag{2}$$

where, the factor $M(\sigma)$ describes the effects of $\alpha$ crystallites ODF on the attenuation, and is dependent upon the texture parameter, $\sigma$, which accounts for the distribution width of $\alpha$ crystallites orientations. Two extreme scenarios are described below: When $\sigma \to 0$, $\alpha$ crystallites in each MTC have the identical orientation, and the MTC becomes an $\alpha$-phase single crystallite. Therefore, the attenuation by $\alpha$ crystallites vanishes and $M(\sigma) = 0$. When $\sigma \to \infty$, $\alpha$ crystallites in the MTC have a random and arbitrary orientation distribution. Therefore, the MTCs are absent, and $M(\sigma) = 1$. Following a series of works by Yang et al. [15,47,48], for MTCs with a random and arbitrary distribution

of preferred orientations, $M(\sigma)$ can be calculated by the covariance of the elastic tensor perturbations $\Xi_{11}^{11}(\sigma) = \langle \delta C_{11} \delta C_{11} \rangle$ devided by its asymptote value when $\sigma \to \infty$, i.e., $M(\sigma) = \Xi_{11}^{11}(\sigma) / \lim_{\sigma \to \infty} \Xi_{11}^{11}(\sigma)$. Here, $\Xi_{11}^{11}(\sigma)$ is given by [15]:

$$\begin{aligned} \Xi_{11}^{11}(\sigma) \quad &= 3\left(2A^{\alpha Ti} + 4B^{\alpha Ti}\right) M_3 + 30 D^{\alpha Ti}\left(2A^{\alpha Ti} + 4B^{\alpha Ti}\right) M_2 + 105\left(D^{\alpha Ti}\right)^2 M_4 \\ &- \left[\left(2A^{\alpha Ti} + 4B^{\alpha Ti}\right) M_1 + 3D^{\alpha Ti} M_3\right]^2, \end{aligned} \tag{3}$$

where, the coefficients $A^{\xi}$, $B^{\xi}$, and $D^{\xi}$ are defined in terms of single crystallite elastic constants $C_{ij}^{\xi}$ of the medium $\xi$($\xi = \alpha Ti$ in Equation (3)) as:

$$\begin{aligned} A^{\xi} &= C_{13}^{\xi} - C_{12}^{\xi} \\ B^{\xi} &= C_{44}^{\xi} - C_{66}^{\xi} \\ D^{\xi} &= C_{11}^{\xi} + C_{33}^{\xi} - 2C_{13}^{\xi} - 4C_{44}^{\xi}, \end{aligned} \tag{4}$$

Here, the parameters $M_i$ are dependent upon the texture parameter $\sigma$, and are expressed by:

$$\begin{aligned} M_1 &= \tfrac{1}{2}\left(I_\sigma^0 - I_\sigma^2\right) \\ M_2 &= \tfrac{1}{48}\left(I_\sigma^0 - 3I_\sigma^2 + 3I_\sigma^4 - I_\sigma^6\right) \\ M_3 &= \tfrac{1}{8}\left(I_\sigma^0 - 2I_\sigma^2 + I_\sigma^4\right) \\ M_4 &= \tfrac{1}{384}\left(I_\sigma^0 - 4I_\sigma^2 + 6I_\sigma^4 - 4I_\sigma^6 + I_\sigma^8\right), \end{aligned} \tag{5}$$

with

$$I_\sigma^m = \frac{1}{2}\int_0^\pi F(\sigma, \theta) \cos^m \theta \sin\theta d\theta, \tag{6}$$

where $F(\sigma, \theta)$ accounts for the ODF of $\alpha$ crystallites, with $\theta$ denoting the misorientation angle between crystallites. It can be represented by a Gaussian-like distribution function, which has been demonstrated to fit the experimental OIM data well [49]:

$$F(\sigma, \theta) = \frac{1/\sigma}{e^{1/(2\sigma)} - e^{-1/(2\sigma)}} e^{\left(\frac{\cos\theta}{2\sigma}\right)}. \tag{7}$$

Following the classical Weaver's theoretical model [50], the grain scattering-induced attenuation of longitudinal waves propagating in an equiaxed hexagonal polycrystalline material can be given by [48]:

$$\alpha_L^{\xi} = \alpha_{LL}^{\xi} + \alpha_{LT}^{\xi}, \tag{8}$$

with

$$\alpha_{IJ}^{\xi} = \frac{8\pi^4 f^4 a^3}{v_I^3 v_J^5 \rho^2} \int_{-1}^{+1} \frac{IP_{IJ}^{\xi}(\cos\gamma)}{\left[1 + (k_I a)^2 + \left(k_J a\right)^2 - 2(k_I a)\left(k_J a\right)(\cos\gamma)\right]^2} d(\cos\gamma). \tag{9}$$

Here, the subscripts $L$ denotes the total attenuation of longitudinal waves, the notation $IJ = LL$ or $LT$ represents the wave mode conversion between longitudinal ('$L$') and transverse ('$T$') waves during ultrasonic wave scattering at grain boundaries. $\xi$ denotes the fields related to the medium $\xi$, and $\xi = \alpha Ti$ or $MTC$. $k_{\xi'}$ and $v_{\xi'}$ define the propagation constant and the ultrasonic velocity of the wave mode $\xi'$, respectively. $\rho$ is the density of the material. $a$ is the mean chord length, and is usually defined as half of the mean grain diameter, $\overline{D}/2$. $\gamma$ is the scattering angle. $IP_{IJ}^{\xi}$ accounts for the effects of elastic properties

of the medium $\xi$ on ultrasonic scattering-induced attenuation. It is usually defined as the tensorial inner product, and is expressed by [48]:

$$IP_{IJ}^{\xi} = A_{IJ}^{\xi} + B_{IJ}^{\xi}(\cos\gamma)^2 + C_{IJ}^{\xi}(\cos\gamma)^4, \tag{10}$$

where, the coefficients $A_{IJ}^{\xi}$, $B_{IJ}^{\xi}$ and $C_{IJ}^{\xi}$ are related to the elastic constants of a single crystallite of the medium $\xi$.

$$\begin{aligned}
A_{LL}^{\xi} &= \tfrac{4}{45}\left(A^{\xi}\right)^2 + \tfrac{8}{1575}\left(D^{\xi}\right)^2 + \tfrac{8}{315}A^{\xi}D^{\xi} \\
B_{LL}^{\xi} &= \tfrac{4}{15}\left(A^{\xi}\right)^2 + \tfrac{16}{15}\left(B^{\xi}\right)^2 + \tfrac{92}{1575}\left(D^{\xi}\right)^2 + \tfrac{64}{45}A^{\xi}B^{\xi} + \tfrac{32}{63}B^{\xi}D^{\xi} + \tfrac{88}{315}A^{\xi}D^{\xi} \\
C_{LL}^{\xi} &= -C_{LT}^{\xi} = \tfrac{16}{45}\left(B^{\xi}\right)^2 + \tfrac{4}{252}\left(D^{\xi}\right)^2 + \tfrac{32}{315}B^{\xi}D^{\xi} \\
A_{LT}^{\xi} &= \tfrac{8}{15}\left(A^{\xi}\right)^2 + \tfrac{4}{15}\left(B^{\xi}\right)^2 + \tfrac{2}{105}\left(D^{\xi}\right)^2 + \tfrac{4}{15}A^{\xi}B^{\xi} + \tfrac{4}{35}B^{\xi}D^{\xi} + \tfrac{8}{105}A^{\xi}D^{\xi} \\
B_{LT}^{\xi} &= \tfrac{28}{45}\left(B^{\xi}\right)^2 + \tfrac{32}{1575}\left(D^{\xi}\right)^2 + \tfrac{4}{15}A^{\xi}B^{\xi} + \tfrac{68}{315}B^{\xi}D^{\xi} + \tfrac{4}{105}A^{\xi}D^{\xi}.
\end{aligned} \tag{11}$$

It is remarked that the effective elastic constants of MTCs are dominated by the texture parameter $\sigma$, and are calculated by:

$$\begin{aligned}
C_{11}^{MTC} &= C_{12}^{\alpha Ti} + 2C_{66}^{\alpha Ti} + \left(2A^{\alpha Ti} + 4B^{\alpha Ti}\right)M_1 + 3D^{\alpha Ti}M_3 \\
C_{12}^{MTC} &= C_{12}^{\alpha Ti} + 2A^{\alpha Ti}M_1 + D^{\alpha Ti}M_3 \\
C_{13}^{MTC} &= C_{12}^{\alpha Ti} + 2A^{\alpha Ti}(2M_1 + M_6) + D^{\alpha Ti}M_7 \\
C_{44}^{MTC} &= C_{66}^{\alpha Ti} + 2B^{\alpha Ti}(2M_1 + M_2) + D^{\alpha Ti}M_7 \\
C_{33}^{MTC} &= C_{12}^{\alpha Ti} + 2C_{66}^{\alpha Ti} + \left(2A^{\alpha Ti} + 4B^{\alpha Ti}\right)(M_1 + M_6) + D^{\alpha Ti}M_5 \\
C_{66}^{MTC} &= 1/2\left(C_{11}^{MTC} - C_{12}^{MTC}\right).
\end{aligned} \tag{12}$$

where, the coefficients $M_i$ are defined as:

$$\begin{aligned}
M_5 &= I_{\sigma}^4 \\
M_6 &= \tfrac{1}{2}\left(-I_{\sigma}^0 + 3I_{\sigma}^2\right) \\
M_7 &= \tfrac{1}{2}\left(I_{\sigma}^2 - I_{\sigma}^4\right).
\end{aligned} \tag{13}$$

Based on the formulas mentioned above, the factor $M(\sigma)$ and its slope are plotted in Figure 8 as solid and dash lines, respectively. The logarithmic scale of the normalized attenuation contributed by $\alpha$ crystallites and MTCs as a function of the normalized frequency, i.e., $\log_{10}(\alpha\overline{D}/2)$ versus $\log_{10}(k_0\overline{D}/2)$, with three texture parameters $\sigma$ of 0.01, 0.1 and 1 are plotted in Figure 9. The elastic constants of a single $\alpha$ crystallite in Equation (4) are taken from [32], and the elastic constants of MTCs determined by Equation (12) for three texture parameters $\sigma$ of 0.01, 0.1 and 1 are listed in Table 3. It is seen that $M$ monotonically increases with the increase of the width of the crystallite ODF. Specifically, $M$ is smaller than 0.001 when $\sigma \leq 0.02$. It means that the attenuation contributed by the fine $\alpha$ crystallites can be negligible as compared to the contribution of the coarse MTCs for a microstructure with a narrow ODF distribution (as shown by an example of $\sigma = 0.01$ in Figure 9a). Furthermore, when $\sigma$ is in the range of [0.02, 1), the factor $M$ increases rapidly, indicating that the contribution by the fine $\alpha$ crystallites is more and more significant, and becomes comparable with the contribution of MTCs (as shown by an example of $\sigma = 0.1$ in Figure 9b). Finally, the factor $M$ tends to 1 when $\sigma \geq 2$, indicating that the fine $\alpha$ crystallites make a major contribution to the total attenuation (as shown by an example of $\sigma = 1$ in Figure 9c).

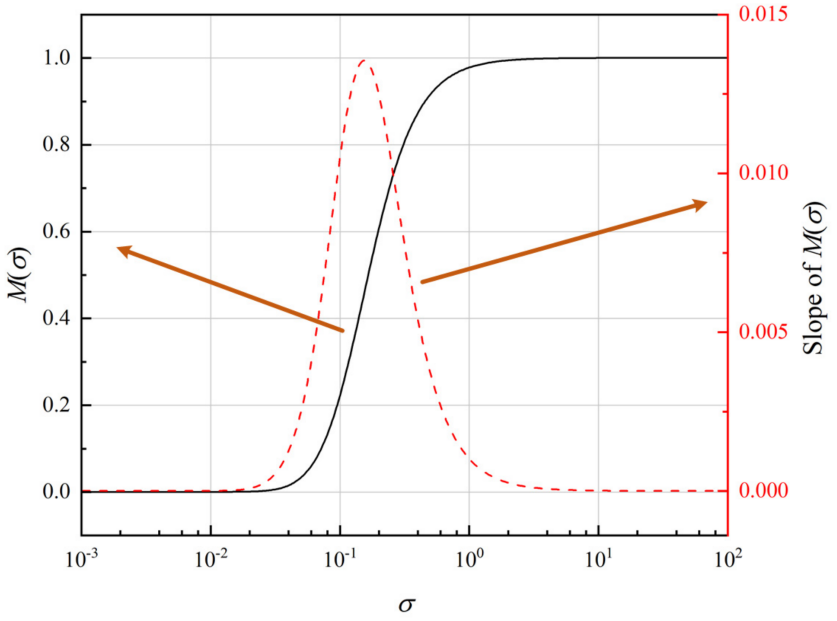



**Figure 8.** The factor $M(\sigma)$ as a function of the texture parameter $\sigma$ (solid line) and its slope (dash line).

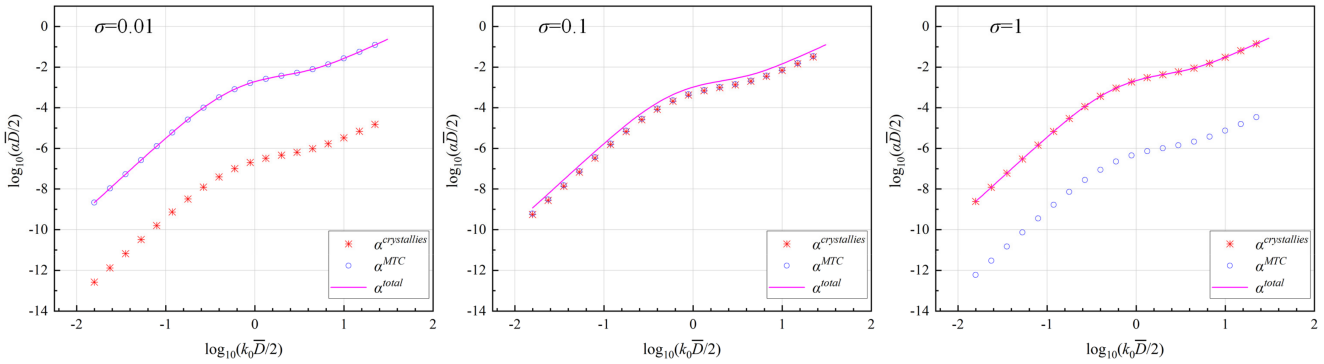



**Figure 9.** The logarithmic scale of the normalized attenuation as a function of the normalized frequency, i.e., $\log_{10}(\alpha\overline{D}/2)$ vs. $\log_{10}(k_0\overline{D}/2)$, for the total attenuation ($\alpha^{total}$), the attenuation contributed by α crystallites ($\alpha^{crystallies}$), and by MTCs ($\alpha^{MTC}$) with three texture parameters $\sigma$. (**a**) $\sigma = 0.01$; (**b**) $\sigma = 0.1$; (**c**) $\sigma = 1$.

**Table 3.** Elastic constants for α crystallites and MTCs with different texture parameters $\sigma$ .

| | | | Elastic Constants (GPa) | | | | | |
|---|---|---|---|---|---|---|---|---|
| | | | $C_{11}$ | $C_{12}$ | $C_{13}$ | $C_{33}$ | $C_{44}$ | $C_{66}$ |
| α crystallites [32] | | | 154.24 | 86.76 | 63.62 | 174.45 | 44.30 | 33.74 |
| MTCs | Composite specimens | $\sigma = 7.5\times10^{-4}$ | 154.23 | 86.69 | 63.69 | 174.43 | 44.32 | 33.77 |
| | Artifical cases | $\sigma = 0.01$ | 154.19 | 85.86 | 64.51 | 172.78 | 44.53 | 34.16 |
| | | $\sigma = 0.1$ | 155.11 | 79.86 | 69.19 | 164.26 | 44.47 | 37.62 |
| | | $\sigma = 1$ | 157.65 | 73.16 | 72.84 | 157.93 | 42.47 | 42.25 |

The distribution of the misorientation angle $\theta$ obtained by using the OIM technique was fitted by using the normalized Gaussian-like orientation function $e^{\cos(\theta)/(2\sigma)}/e^{1/(2\sigma)}$. The OIM-determined distribution histogram and the fitted curve are plotted in Figure 10. Results exhibit a goodness of fit with the coefficient of determination $R^2$ of 0.82. The fitted texture parameter $\sigma$ is equal to $7.5 \times 10^{-4}$, indicating that the studied composite material

has an extremely narrow orientation distribution, and thus the anisotropy degree of the coarse MTCs is strong. In this case, the elastic constants of MTCs are demonstrated to be indistinguishable from those of α crystallites (seen in Table 3). Furthermore, analytical results for the attenuation contributed by α crystallites and MTCs are calculated for all the three Ti6Al4V/$B_4C$ composite specimens given that the mean grain size is known from the EBSD observations (Figure 11). It is obvious that the order of magnitude of the attenuation caused by α crystallites is much smaller than that caused by MTCs at a given frequency. Thus, the attenuation caused by α crystallites makes an insignificant contribution to the total scattering-induced attenuation and can be neglected. Therefore, the attenuation and the spectral centroid frequency shift measured by ultrasonic inspection are mainly associated with the size, morphology and elastic properties of coarse MTCs.

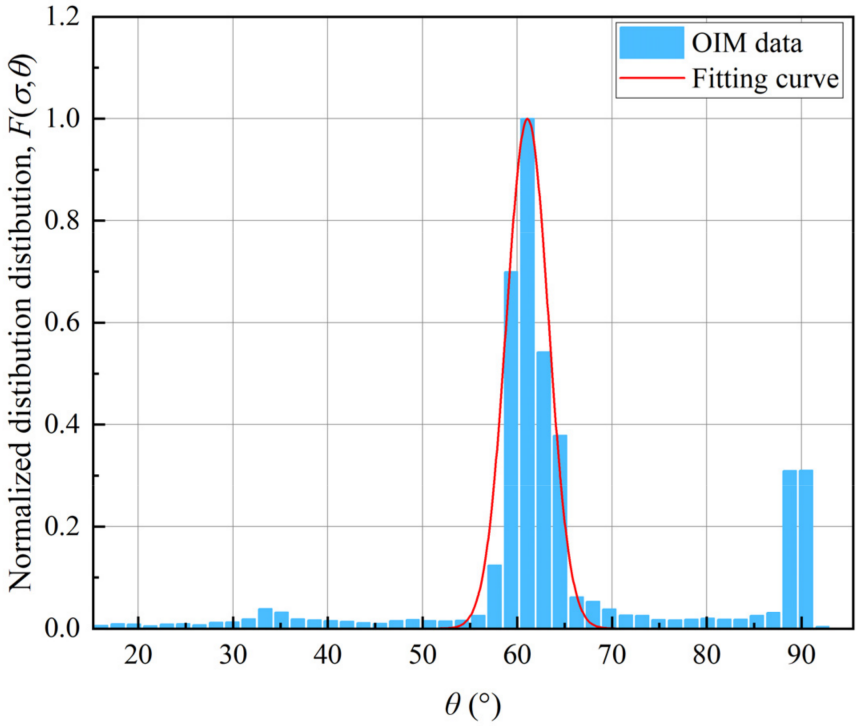



**Figure 10.** The OIM-determined orientation distribution histogram and the fitted curve by using the normalized Gaussian-like orientation function $e^{\cos(\theta)/(2\sigma)}/e^{1/(2\sigma)}$. The fitted texture parameter $\sigma$ is equal to $7.5 \times 10^{-4}$ with the fitted coefficient of determination $R^2$ of 0.82.

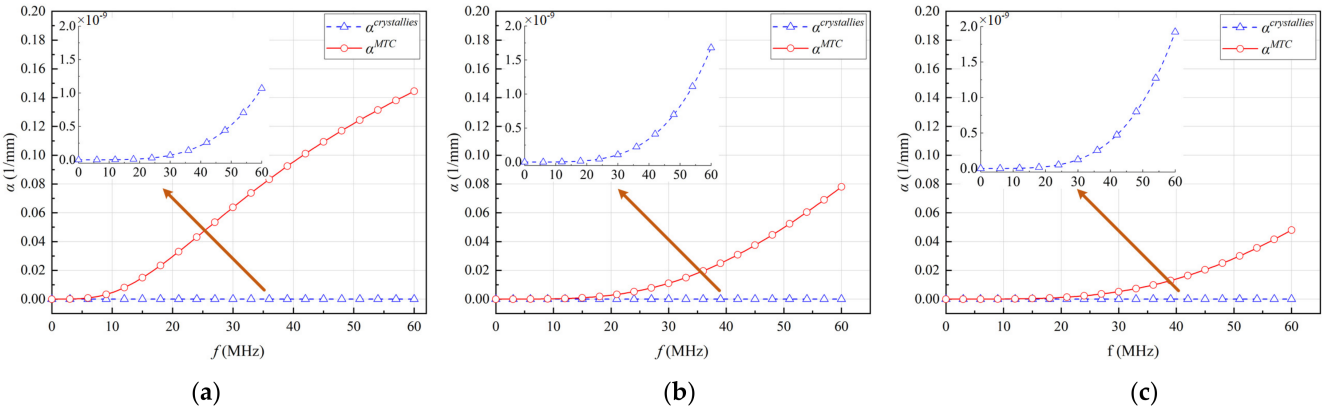



**Figure 11.** The attenuation coefficients contributed by α crystallites and MTCs in all the three Ti6Al4V/$B_4C$ composite specimens. (**a**) TMC1; (**b**) TMC2; (**c**) TMC3.

### 3.2. Centroid Frequency Downshift

The amplitude or power spectra of the ultrasonic signals can be assumed to have a Gaussian shape in most industrial non-destructive testing applications. The spectra would remain a Gaussian shape during the ultrasonic wave propagation no matter what the scattering regime is. However, the spectral centroid frequency of signals will downshift since the high-frequency components experience a lager attenuation than the low-frequency ones, and the spectral centroid frequency of ultrasonic echoes can be written as [26]:

$$f_r = \frac{f_i - 2c_2\sigma_i^2 b\overline{D}^{n-1}z}{1 + 2c_1\sigma_i^2 b\overline{D}^{n-1}z}, \tag{14}$$

with

$$\begin{aligned} c_1 &= \tfrac{n(n-1)}{2} f_i^{n-2} \\ c_2 &= n(2-n) f_i^{n-1}, \end{aligned} \tag{15}$$

where $f_i$ and $f_r$ denote the centroid frequencies of the incident and the received pulse signals' spectra. $z$ denotes the propagation distance. $\sigma_i^2$ and $\sigma_r^2$ denote the variance of the incident and the received pulse's spectra. The exponent $n$ is closely related to the scattering regime and is generally in the range of 0-4. It is defined by the classical exponential form of the attenuation coefficient $\alpha(f) = b\overline{D}^{n-1}f^n$ [23,50,51], where $b$ represents the linear scaling factor depending on the elastic constants and the density. Equation (14) gives the relationship between the mean grain size and the centroid frequency of the received signal's spectrum. When the exponent $n = 2$, i.e., a quadratic frequency dependence of attenuation, which could often be observed in the ultrasonic nondestructive evaluation of polycrystalline microstructures [27,30,52,53], Equation (14) can be rewritten as:

$$f_r = \frac{f_i}{1 + 2\sigma_i^2 b\overline{D}z}. \tag{16}$$

Because of the noise created during the laser generation process, the incident wave maybe not readily available. Then the ratio between the spectral centroid frequencies of two successive transmitted/reflected echoes can be used to evaluate the mean grain size. Actually, for the two successive transmitted/reflected echoes, corresponding to the spectral centroid frequencies $f_{r1}$, $f_{r2}$, and the propagation distances $z_1$, $z_2$(assuming $z_2 > z_1$), in the case of $n = 2$, we have:

$$\frac{f_{r1}}{f_{r2}} = 1 + \frac{2\sigma_i^2 b\overline{D}(z_2 - z_1)}{1 + 2\sigma_i^2 b\overline{D}z_1}. \tag{17}$$

Based on the relationship between the variances of the received and incident pulses' spectra, $\sigma_{r1}^2 = \frac{\sigma_i^2}{1+2\sigma_i^2 b\overline{D}z_1}$ [38], Equation (17) can be simplified as:

$$\frac{f_{r1}}{f_{r2}} = 1 + 2\sigma_{r_1}^2 b\overline{D}(z_2 - z_1). \tag{18}$$

Equation (18) provides an explicit formula for the correlation of the mean grain size and the centroid frequency ratio between the two successive echo signals propagating in a polycrystalline material with a quadratic frequency dependence of attenuation. It is indicated, at least theoretically, that the ratio between the centroid frequencies of the two successive echoes, $f_{r1}/f_{r2}$, is linearly related to the mean grain size of the material. The experimental investigation in the following section would verify the validity of this theoretical model.

In addition, it is well known that the grain scattering-induced attenuation is dominated by the grain volume in the Rayleigh region ($n = 4$), and by the dimension along the ultrasonic wave propagation direction in the stochastic region ($n = 2$) [54]. Since the attenuation caused by MTCs corresponds to the Rayleigh-to-stochastic transition region, it

would be influenced by not only the volume but also the morphology of MTCs. Obviously, the dimension along the deposition direction (i.e., the ultrasonic wave propagation direction) of Ti6Al4V specimens composed of columnar MTCs is much larger than the one of Ti6Al4V/$B_4C$ composite specimens composed of equiaxed MTCs. Thus, the attenuation and the centroid frequency shift in Ti6Al4V and Ti6Al4V/$B_4C$ composite specimens should not be compared with each other.

## 4. Results and Discussion

### *4.1. Correlation of Ultrasonic Velocity to Microstructural Properties*

Correlation between the ultrasonic longitudinal wave velocity and the microstructural properties of the Ti6Al4V/$B_4C$ composites is first analyzed. A typical laser ultrasonic transmission waveform is shown in Figure 12. The laser-generated ultrasonic longitudinal wave arrived at the detection surface for the first time at near $t$ = 1.5 μs, corresponding to the first transmitted longitudinal pulse echo, i.e., 1L. After about 3.2 μs, the pulse echo arriving at the detection surface for the second time, i.e., 2L, was measured. It is worth noting that the initial moment of the generated signal is not the point corresponding to the time at $t$ = 0 μs. Instead, the longitudinal wave velocity should be determined by the relative time difference in the arrival time of the first and the second pulse echoes.

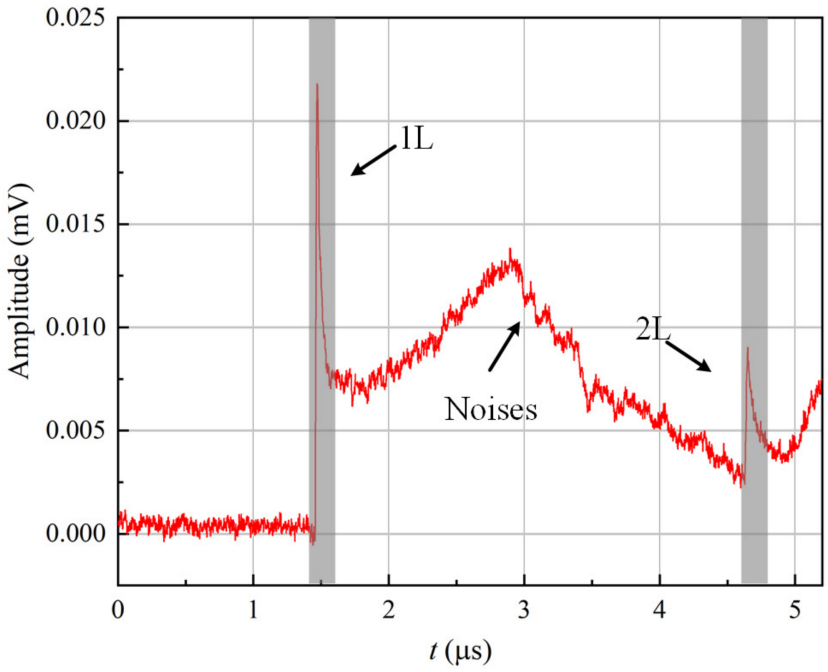



**Figure 12.** Example of laser ultrasonic waveforms.

The crosscorrelation time delay measurement method is used for calculating ultrasonic velocity. Actually, the initial time of an incident laser pulse cannot be accurately measured due to the influence of the electronic circuit of ultrasonic detection system and the delay of triggering system. The crosscorrelation method does not require the knowledge of the initial time of the incident laser pulse and the exact arrival time of the echo signals. It takes advantage of the similarity of the two successive transmitted/reflected echoes to reduce the effect of local uncorrelated noises [55]. It is demonstrated that this method can give reliable and reproducible results even in difficult cases when the material is a highly attenuating medium, or where the transmitted/reflected echoes are noisy and distorted [55–57].

The signal processing procedures by use of the crosscorrelation method can be described as follows: Select the 1L and 2L signals (as shown in the shaded part of Figure 12), whose starting times are noted as $t_{1L}$ and $t_{2L}$. Then filter out the direct current and the high-frequency noise components. After denoising, the two longitudinal wave echo signals

are normalized to the same energy and are corrected according to their mean values. Their crosscorrelation is then calculated using a spline-interpolation algorithm at uniform intervals of $t_s/25$ in order to minimize the error caused by the sampling frequency limitation. Here, $t_s$ denotes the sampling interval. The time delay between these two successive echoes is eventually measured by $\Delta t = t_{2L} - t_{1L} + \Delta t_f$, where $\Delta t_f$ defines the fine time delay given by the maximum value of the crosscorrelation curve [55]. Therefore, the longitudinal wave velocity is estimated by $v_l = (z_{2L} - z_{1L})/\Delta t$. Here, $z_{1L}$ and $z_{2L}$ denote the propagation distances corresponding to the longitudinal arrivals of 1L and 2L, respectively.

Since the crystallographic orientation of each crystallite is known based on EBSD observations, the phase velocity in each crystallite can be calculated by the eigenvalue of the determinant of the Christoffel equation [58]. Theoretically, the ultrasonic velocity in the specimen can be obtained by the Voigt average of phase velocity in each crystallite, yielding the result of 5978.5 m/s. Laser-ultrasonic inspection results of the ultrasonic longitudinal wave velocity measured by the average value of five different points for each specimen have been given in Table 4. It is shown that experimental results have a maximum deviation of 2.23% from the theoretical result, and this is in good agreement with the anisotropy degree of the specimens as shown in Figure 6. It seems that the longitudinal wave velocity decreases as the size of MTCs decreases. Nevertheless, the variation in ultrasonic velocity becomes less sensitive to the specimens of TMC2 and TMC3 with smaller MTCs. This may bring large errors to grain size evaluation by inversion of ultrasonic longitudinal wave velocity for specimens with small grain size.

**Table 4.** Longitudinal wave velocity in the composite specimens.

| Specimens | Experiment Estimations(m/s) | Deviation from Theoretical Results (%) |
|---|---|---|
| TMC1 | $6112.0 \pm 7.7$ | 2.23 |
| TMC2 | $6083.2 \pm 6.2$ | 1.75 |
| TMC3 | $6083.4 \pm 9.1$ | 1.75 |

### *4.2. Correlation of Centroid Frequency Downshift to Microstructural Properties*

Averaged results of different measurement points on each specimen were used for the correlation analysis between the mean size of MTCs and the centroid frequency shift. The rectangular window function was used to acquire each pulse echo signal whose duration was about 0.04 μs (shown as the gray parts in Figure 13). Filtering the direct current and the high-frequency noises, the discrete Fourier transform was applied to obtain the frequency domain information of the acquired pulse echo. The amplitude spectrum of each received pulse echo was fitted using the Gaussian model by means of the nonlinear regression analysis within the confidence frequency range of 5–55 MHz. The centroid frequency of the fitted 1L and 2L are noted as $f_{r1}$ and $f_{r2}$ (as shown in Figure 13). A good fit for the spectra of both 1L and 2L pulse echoes by using the Gaussian model has been obtained, with coefficients of determination ($R^2$) all above 0.98 and root mean square errors all below 0.001.

Standard deviation and mean estimations of the centroid frequency shift for each specimen are shown in Table 5. Correlation and linear fitting analysis between the mean size of MTCs and the centroid frequency shift are further conducted, as shown in Figure 14. The results show that the centroid frequency shift increases with the increase of the mean size of MTCs. In fact, larger MTCs show a greater attenuation level at high frequencies, so the centroid frequency of the signal's spectrum experiences a greater downshift during ultrasonic wave propagation. It is seen from Figure 14 that the centroid frequency shift and the mean size of MTCs show similar variation trends. The results exhibit a goodness of linear fit with $R^2 = 0.992$, suggesting that the centroid frequency shift is approximately linear to the mean size of MTCs. This result verifies the theoretical prediction in Equation (18). Furthermore, the standard deviations of the centroid frequency shift among different measurements for each specimen are plotted as vertical error bars in Figure 14. It is shown that the deviation level from the average is greater for the specimen with a larger size of

MTCs. Moreover, compared with the ultrasonic velocity method, the centroid frequency shift method is more sensitive to the variation of smaller MTCs, having greater potentials in improving the accuracy in the characterization of the MTC size.

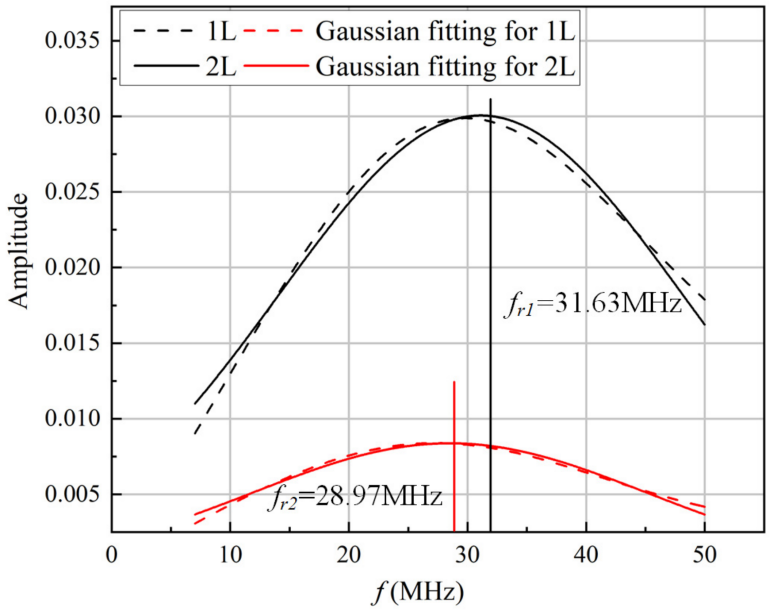



**Figure 13.** The amplitude spectra and Gaussian fit curves of 1L and 2L pulse echoes.

**Table 5.** Standard deviations and mean estimations of the centroid frequency shift in Ti6Al4V/$B_4C$ composite specimens.

| Samples | $f_{r1}/f_{r2}$ | | $\overline{\sigma}_{r1}$ (MHz) |
|---|---|---|---|
| | Mean Value | Standard Deviation | |
| TMC1 | 1.067 | 0.0278 | 16.839 |
| TMC2 | 1.043 | 0.0229 | 16.978 |
| TMC3 | 1.039 | 0.0135 | 15.966 |

It can be concluded that, for a macroscopically untextured near-α titanium alloy, the ultrasonic velocity is actually closely related to the Voigt averaged velocity of α-phase fine crystallites, and is not correlated with the texture parameter of MTCs. Therefore, the ultrasonic velocity is insensitive to the size of MTCs. While the spectral centroid frequency downshift of the received echoes is closely related to the texture parameter of MTCs. When the texture parameter is smaller than 0.02, i.e., the crystallographic ODF distribution is relatively narrow, the contribution of fine α crystallites to the spectral centroid frequency downshift is insignificant as compared to the contribution of coarse MTCs. In this case, the measured spectral centroid frequency downshift is dominated by the size and morphology of MTCs. This has been verified by the linear relationship between centroid frequency downshift and the size of MTCs obtained by our laser-ultrasonic experiment. With the increase of the texture parameter, the contributions of fine α crystallites and coarse MTCs to the centroid frequency downshift are of the same order, and the correlation between ultrasonic characteristics and microstructural properties becomes complex. This case will be further studied.

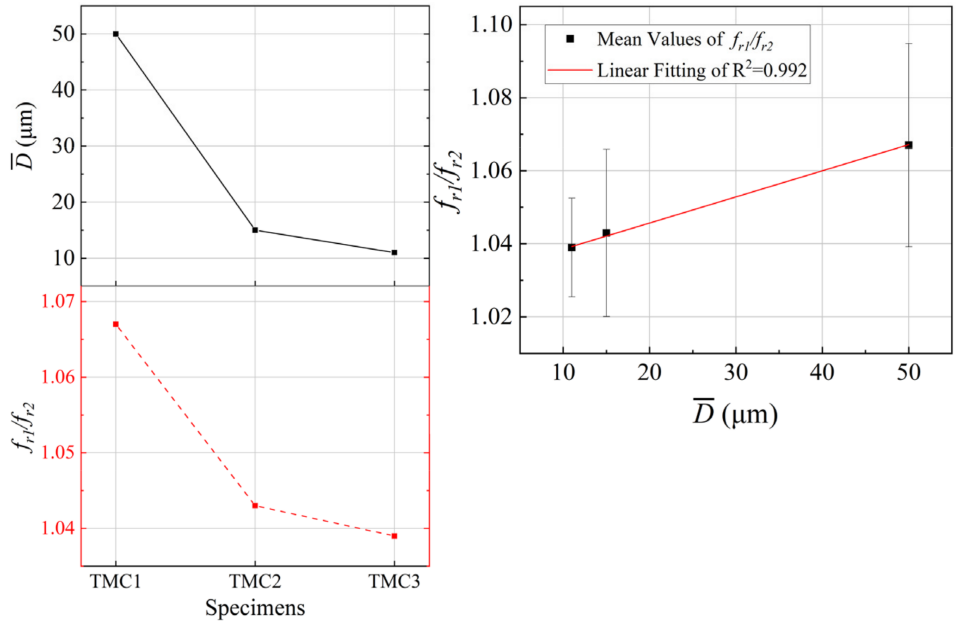



**Figure 14.** Correlation analysis between mean size of MTCs and centroid frequency shift of Ti6Al4V/$B_4C$ composite specimens. (**a**) The mean size of MTCs measured by EBSD (solid line), and the centroid frequency shift (dash line). (**b**) Linear fitting for the centroid frequency shift as a function of the mean size of MTCs.

## 5. Conclusions

Laser melting deposited Ti6Al4V/$B_4C$ composite specimens composed of approximately equiaxed MTCs formed by finer α crystallites with preferred orientations were obtained by adding an amount of nano-sized $B_4C$ particles to the original Ti6Al4V powder. Theoretical investigations showed the scattering-induced attenuation and the spectral centroid frequency downshift were closely related with the texture parameter, $\sigma$, which accounts for the crystallographic orientation distribution width. By the Gaussian-like function fitting, it was found that the studied composite had an extremely small value of $\sigma$, indicating a strong anisotropy degree in each MTC. Therefore, the scattering-induced attenuation and the spectral centroid frequency downshift were mainly determined by the size, morphology and elastic properties of MTCs, and the contribution of fine α-phase crystallites was neglected. The correlation between laser-generated ultrasonic wave properties and microstructural properties of Ti6Al4V/$B_4C$ composites was analyzed. Experimentally estimated ultrasonic velocity showed a maximum deviation of 2.23% from the theoretical result determined by the Voigt-averaged velocity in each crystallite, and this deviation was attributed to the macroscopically anisotropy degree observed in the composite specimens by the EBSD technique. Nevertheless, the ultrasonic velocity seemed to be insensitive to the size of MTCs. Furthermore, an approximate linear relationship between the spectral centroid frequency downshift and the mean size of MTCs was found with a goodness-of-fit ($R^2$) up to 0.99. The results provided would help support the nondestructive evaluation of the grain size and the fatigue properties in 3D printed metal composite materials using laser ultrasonic technology.

**Author Contributions:** Conceptualization, W.X. and X.B.; methodology, W.X. and X.B.; software, W.X.; validation, W.X. and X.B.; formal analysis, W.X. and Z.G.; investigation, X.B.; resources, Z.S. and X.M.; data curation, W.X.; writing—original draft preparation, W.X.; writing—review and editing, X.B.; visualization, W.X. and X.M.; supervision, X.B. and Z.S.; project administration, X.B.; funding acquisition, X.B. All authors have read and agreed to the published version of the manuscript.

**Funding:** This research was funded by National Natural Science Foundation of China, grant number 51805304, the Major Scientific and Technological Innovation Projects in Shandong Province, grant number 2019JZZY010418, the Natural Science Foundation of Shandong Province, grant number ZR2019PEE014, Qilu University of Technology (Shandong Academy of Science) science, education and industry integration innovation pilot project (international cooperation), grant number 2020KJC-GH12, Youth Foundation Project of Shandong Academy of Sciences, grant number 2020QN004, "University 20" Innovation Team Project of Jinan, grant number 2020GXRC004 and Qilu University of Technology (Shandong Academy of Science) Computer Science and Technology Basic Research Promotion Project, grant number 2021JC02008.

**Institutional Review Board Statement:** Not applicable.

**Informed Consent Statement:** Not applicable.

**Data Availability Statement:** The processed data required to reproduce these findings cannot be shared at this time as the data also forms part of an ongoing study, although they will be made available on request.

**Conflicts of Interest:** The authors declare no conflict of interest.

## Nomenclature

| | |
|---|---|
| $\overline{D}$ | The mean size of grains |
| $\overline{A}$ | The arithmetic average of grain areas |
| $\alpha^{total}$ | Total ultrasonic scattering-induced attenuation |
| $\alpha^{crystallites}$ | Attenuation caused by the fine $\alpha$ crystallites |
| $\alpha^{MTC}$ | Attenuation caused by the coarse microtextured clusters (MTC) |
| $\alpha^{\alpha Ti}$ | Attenuation caused by a macroscopically isotropic and homogeneous $\alpha$-phase polycrystalline titanium |
| $\sigma$ | Texture parameter accounting for the distribution width of $\alpha$ crystallite orientations |
| $M(\sigma)$ | The factor accounting for the effects of $\alpha$ crystallite orientation distribution function (ODF) on the attenuation |
| $\xi$ | The fields related to the medium $\xi$.$\xi = \alpha Ti$ denotes a macroscopically isotropic and homogeneous $\alpha$-phase polycrystalline titanium, and $\xi = MTC$ denotes the medium of MTCs |
| $C_{ij}^{\xi}$ | Single crystallite elastic constants of the medium $\xi$ |
| $\Xi_{11}^{11}(\sigma)$ | The covariance of the elastic tensor perturbations as a function of $\sigma$ |
| $A^{\xi}$, $B^{\xi}$, $D^{\xi}$ | Coefficients defined in terms of $C_{ij}^{\xi}$ |
| $M_i$ | Parameters dependent upon $\sigma$ |
| $\theta$ | The misorientation angle between crystallites |
| $\gamma$ | Scattering angle |
| $k_{\xi'}$ | The propagation constant of the wave mode $\xi'$ |
| $v_{\xi'}$ | The ultrasonic velocity of the wave mode $\xi'$ |
| $\rho$ | The density of the material |
| $IP_{IJ}^{\xi}$ | The effects of elastic properties of the medium $\xi$ on ultrasonic attenuation |
| $A_{IJ}^{\xi}$, $B_{IJ}^{\xi}$, $C_{IJ}^{\xi}$ | Coefficients related to the single crystallite elastic constants of the medium $\xi$; |
| $a$ | The mean chord length |
| $n$ | The exponent closely related to the scattering regime |
| $b$ | The linear scaling factor depending on the elastic constants and the density |
| $c_i$ | Coefficients related to the exponent $n$ and the frequency |
| $f_i$, $f_r$ | The spetral centroid frequencies of the incident and received pulses' spectra |
| $\sigma_i^2$, $\sigma_r^2$ | The variances of the incident and received pulses' spectra |
| $f_{r1}$, $f_{r2}$ | The spectral centroid frequencies of the first and second received echoes |
| $z_1$, $z_2$ | The propagation distances of the the first and second received echoes |

## References


1. Shah, K.; Pinkerton, A.J.; Salman, A.; Li, L. Effects of Melt Pool Variables and Process Parameters in Laser Direct Metal Deposition of Aerospace Alloys. *Mater. Manuf. Process.* **2010**, *25*, 1372–1380. [CrossRef]
2. Lopez, A.; Bacelar, R.; Pires, I.; Santos, T.G.; Sousa, J.P.; Quintino, L. Non-Destructive Testing Application of Radiography and Ultrasound for Wire and Arc Additive Manufacturing. *Addit. Manuf.* **2018**, *21*, 298–306. [CrossRef]
3. Pinkerton, A.J.; Karadge, M.; Ul Haqsyed, W.; Li, L. Thermal and Microstructural Aspects of the Laser Direct Metal Deposition of Waspaloy. *J. Laser Appl.* **2006**, *18*, 216–226. [CrossRef]
4. Khorasani, M.; Ghasemi, A.; Rolfe, B.; Gibson, I. Additive Manufacturing a Powerful Tool for the Aerospace Industry. *Rapid Prototyp. J.* **2021**. [CrossRef]
5. Huang, Y.; Leu, M.C.; Mazumder, J.; Donmez, A. Additive Manufacturing: Current State, Future Potential, Gaps and Needs, and Recommendations. *J. Manuf. Sci. Eng.* **2015**, *137*, 014001. [CrossRef]
6. Kulkarni, J.D.; Goka, S.B.; Parchuri, P.K.; Yamamoto, H.; Ito, K.; Simhambhatla, S. Microstructure Evolution Along Build Direction for Thin-wall Components Fabricated with Wire-direct Energy Deposition. *Rapid Prototyp. J.* **2021**, *26*, 1503–1513. [CrossRef]
7. Fang, X.; Ren, C.; Zhang, L.; Wang, C.; Huang, K.; Lu, B. A Model of Bead Size Based on the Dynamic Response of Cmt-Based Wire and Arc Additive Manufacturing Process Parameters. *Rapid Prototyp. J.* **2021**, *27*, 741–753. [CrossRef]
8. Tang, S.; Wang, G.; Song, H.; Li, R.; Zhang, H. A Novel Method of Bead Modeling and Control for Wire and Arc Additive Manufacturing. *Rapid Prototyp. J.* **2021**, *27*, 311–320. [CrossRef]
9. Dai, F.; Zhang, H.; Li, R. Process Planning Based on Cylindrical or Conical Surfaces for Five-axis Wire and Arc Additive Manufacturing. *Rapid Prototyp. J.* **2020**, *26*, 1405–1420. [CrossRef]
10. Ke, Y.; Xiong, J. Microstructure and Mechanical Properties of Double-Wire Feed Gta Additive Manufactured 308l Stainless Steel. *Rapid Prototyp. J.* **2020**, *27*, 1289–1301. [CrossRef]
11. Rashid, R.R.; Palanisamy, S.; Attar, H.; Bermingham, M.; Dargusch, M. Metallurgical Features of Direct Laser-Deposited Ti6Al4V with Trace Boron. *J. Manuf. Process.* **2018**, *35*, 651–656. [CrossRef]
12. Davis, A.; Kennedy, J.; Strong, D.; Kovalchuk, D.; Porter, S.; Prangnell, P. Tailoring Equiaxed β-Grain Structures in Ti-6Al-4V Coaxial Electron Beam Wire Additive Manufacturing. *Material* **2021**, *20*, 101202. [CrossRef]
13. Ngo, T.D.; Kashani, A.; Imbalzano, G.; Nguyen, K.T.; Hui, D. Additive Manufacturing (3D Printing): A Review of Materials, Methods, Applications and Challenges. *Compos. Part B Eng.* **2018**, *143*, 172–196. [CrossRef]
14. Fayazfar, H.; Salarian, M.; Rogalsky, A.; Sarker, D.; Russo, P.; Paserin, V.; Toyserkani, E. A Critical Review of Powder-Based Additive Manufacturing of Ferrous Alloys: Process Parameters, Microstructure and Mechanical Properties. *Mater. Des.* **2018**, *144*, 98–128. [CrossRef]
15. Yang, L.; Li, J.; Lobkis, O.; Rokhlin, S. Ultrasonic Propagation and Scattering in Duplex Microstructures with Application to Titanium Alloys. *J. Nondestruct. Eval.* **2012**, *31*, 270–283. [CrossRef]
16. Gil, F.; Planell, J. Behavior of Normal Grain Growth Kinetics in Single Phase Titanium and TITANIUM alloys. *Mat. Sci. Eng. A* **2000**, *283*, 17–24. [CrossRef]
17. Somov, P.A.; Statnik, E.S.; Malakhova, Y.V.; Nyaza, K.V.; Salimon, A.I.; Ryabov, D.K.; Korsunsky, A.M. On the Grain Microstructure–Mechanical Properties Relationships in Aluminium Alloy Parts Fabricated by Laser Powder Bed Fusion. *Metals* **2021**, *11*, 1175. [CrossRef]
18. Hirsekorn, S. *New Procedures in Nondestructive Testing*; Springer: Berlin, Germany, 1983; pp. 265–275.
19. Hirsekorn, S. The Scattering of Ultrasonic Waves by Polycrystals. *J. Acoust. Soc. Am.* **1982**, *72*, 1021–1031. [CrossRef]
20. Ünal, R.; Sarpün, I.H.; Yalım, H.A.; Erol, A.; Özdemir, T.; Tuncel, S. The Mean Grain Size Determination of Boron Carbide ($B_4C$)–Aluminum (Al) and Boron Carbide ($B_4C$)–Nickel (Ni) Composites by Ultrasonic Velocity Technique. *Mater. Charact.* **2006**, *56*, 241–244. [CrossRef]
21. Laux, D.; Cros, B.; Despaux, G.; Baron, D. Ultrasonic study of $UO_2$: Effects of Porosity and Grain Size on Ultrasonic Attenuation and Velocities. *J. Nucl. Mater.* **2002**, *300*, 192–197. [CrossRef]
22. Oezkan, V.; Sarpuen, I.H. Examining with the Sintered Temperature of Mean Grain Size of $B_4C$-Al-Ni Composites by Ultrasonic Techniques. *Acta Phys. Pol. Ser. A Gen. Phys.* **2012**, *121*, 184–186. [CrossRef]
23. Stanke, F.E.; Kino, G.S. A Unified Theory for Elastic Wave Propagation in Polycrystalline Materials. *J. Acoust. Soc. Am.* **1984**, *75*, 665–681. [CrossRef]
24. Nicoletti, D.; Kasper, D. Ultrasonic Attenuation Based on the Roney Generalized Theory and Multiple Power-Law Grain-Size Distributions. *IEEE Trans. Sonics Ultrason.* **1994**, *41*, 144–149. [CrossRef]
25. Dong, F.; Wang, X.; Yang, Q.; Yin, A.; Xu, X. Directional Dependence of Aluminum Grain Size Measurement by Laser-Ultrasonic Technique. *Mater. Charact.* **2017**, *129*, 114–120. [CrossRef]
26. Narayana, P.; Ophir, J. A Closed Form Method for the Measurement of Attenuation in Nonlinearly Dispersive Media. *Ultrason. Imaging* **1983**, *5*, 17–21. [CrossRef]
27. Zeng, F.; Agnew, S.R.; Raeisinia, B.; Myneni, G.R. Ultrasonic Attenuation Due to Grain Boundary Scattering in Pure Niobium. *J. Nondestruct. Eval.* **2010**, *29*, 93–103. [CrossRef]
28. Kube, C.M. Attenuation of Laser Generated Ultrasound in Steel at High Temperatures; Comparison of Theory and Experimental Measurements. *Ultrasonics* **2016**, *70*, 238–240. [CrossRef]

29. Garcin, T.; Schmitt, J.H.; Militzer, M. In-Situ Laser Ultrasonic Grain Size Measurement in Superalloy Inconel 718. *J. Alloys Compd.* **2016**, *670*, 329–336. [CrossRef]
30. Bai, X.; Zhao, Y.; Ma, J.; Liu, Y.; Wang, Q. Grain-Size Distribution Effects on the Attenuation of Laser-Generated Ultrasound in α-Titanium Alloy. *Materials* **2019**, *12*, 102. [CrossRef] [PubMed]
31. Gubernatis, J.; Domany, E.; Krumhansl, J.; Huberman, M. The Born Approximation in the Theory of the Scattering of Elastic Waves by Flaws. *J. Appl. Phys.* **1977**, *48*, 2812–2819. [CrossRef]
32. Han, Y.; Thompson, R. Ultrasonic Backscattering in Duplex Microstructures: Theory and Application to Titanium Alloys. *Metall. Mater. Trans. A* **1997**, *28*, 91–104. [CrossRef]
33. Margetan, F.J.; Thompson, R.B.; Yalda-mooshabad, I. Backscattered microstructural noise in ultrasonic toneburst inspections. *J. Nondestruct. Eval.* **1994**, *13*, 111–136. [CrossRef]
34. Kumar, A.; Jayakumar, T.; Raj, B. Ultrasonic Spectral Analysis for Microstructural Characterization of Austenitic and Ferritic Steels. *Philos. Mag. A* **2000**, *80*, 2469–2487. [CrossRef]
35. Zhang, X.G.; Simpson, W.A.; Vitek, J.M.; Barnard, D.J.; Tweed, L.J.; Foley, J. Ultrasonic Attenuation Due to Grain Boundary Scattering in Copper and Copper-Aluminum. *J. Acoust. Soc. Am.* **2004**, *116*, 109–116. [CrossRef]
36. Bai, X.; Tie, B.; Schmitt, J.; Aubry, D. Finite Element Modeling of Grain Size Effects on the Ultrasonic Microstructural Noise Backscattering in Polycrystalline Materials. *Ultrasonics* **2018**, *87*, 182–202. [CrossRef]
37. Brosey, W.D. *Ultrasonic Determination of Grain Size in Uranium*; Springer: Boston, MA, USA, 1983; pp. 1399–1409.
38. Bai, X.; Zhao, Y.; Ma, J.; Guo, R.; Zhang, H. Grain Size Characterization by Laser-Based Ultrasonics Based on the Centroid Frequency Shift Method. *Mater. Charact.* **2019**, *155*, 109800. [CrossRef]
39. Quan, Y.; Harris, J.M. Seismic Attenuation Tomography Using the Frequency Shift Method. *Geophysics* **1997**, *62*, 895–905. [CrossRef]
40. Yang, P.; Shi, L.; Liang, J.; Shi, Y.; Kang, L. Experimental Research on Ultrasonic Characteristics of TC18 Additive Manufacturing Titanium Alloy. *Aeron. Manuf. Technol.* **2017**, *5*, 33–37. (In Chinese) [CrossRef]
41. Davis, G.; Nagarajah, R.; Palanisamy, S.; Rashid, R.A.R.; Rajagopal, P.; Balasubramaniam, K. Laser Ultrasonic Inspection of Additive Manufactured Components. *Int. J. Adv. Manuf. Technol.* **2019**, *102*, 2571–2579. [CrossRef]
42. Liu, S.; Jia, K.; Wan, H.; Ding, L.; Xu, X.; Cheng, L.; Zhang, S.; Yan, X.; Lu, M.; Ma, G. Inspection of the Internal Defects with Different Size in Ni and Ti Additive Manufactured Components Using Laser Ultrasonic Technology. *Opt. Laser Technol.* **2022**, *146*, 107543. [CrossRef]
43. Ma, Y.; Hu, X.; Hu, Z.; Sheng, Z.; Ma, S.; Chu, Y.; Wan, Q.; Luo, W.; Guo, L. Simultaneous compositional and grain size measurements using laser opto-ultrasonic dual detection for additive manufacturing. *Materials* **2020**, *13*, 2404. [CrossRef]
44. Vazquez, L.; Rodriguez, M.N.; Rodriguez, I.; Alvarez, P. Influence of Post-Deposition Heat Treatments on the Microstructure and Tensile Properties of Ti-6Al-4V Parts Manufactured by CMT-WAAM. *Metals* **2021**, *11*, 1161. [CrossRef]
45. Sela, A.; Soler, D.; Ortiz-de-zarate, G.; Germain, G.; Ducobu, F.; Arrazola, P.J. Inverse Identification of the Ductile Failure Law for Ti6al4v Based on Orthogonal Cutting Experimental Outcomes. *Metals* **2021**, *11*, 1154. [CrossRef]
46. Meng, X.; Min, J.; Sun, Z.; Zhang, W.; Chang, H.; Han, Y. Columnar to Equiaxed Grain Transition of Laser Deposited Ti6Al4V Using Nano-Sized $B_4C$ Particles. *Compos. Part B Eng.* **2021**, *212*, 108667. [CrossRef]
47. Yang, L.; Turner, J.A.; Li, Z. Ultrasonic Characterization of Microstructure Evolution During Processing. *J. Acoust. Soc. Am.* **2007**, *121*, 50–59. [CrossRef]
48. Yang, L.; Lobkis, O.; Rokhlin, S. Explicit Model for Ultrasonic Attenuation in Equiaxial Hexagonal Polycrystalline Materials. *Ultrasonics* **2011**, *51*, 303–309. [CrossRef] [PubMed]
49. Cho, J.; Rollett, A.; Oh, K. Determination of Volume Fractions of Texture Components with Standard Distributions in Euler Space. *Metall. Mater. Trans. A* **2004**, *35*, 1075–1086. [CrossRef]
50. Weaver, R.L. Diffusivity of Ultrasound in Polycrystals. *J. Mech. Phys. Solids* **1990**, *38*, 55–86. [CrossRef]
51. Ghoshal, G.; Turner, J.A. Numerical Model of Longitudinal Wave Scattering in Polycrystals. *IEEE Trans. Sonics Ultrason.* **2009**, *5*, 1419–1428. [CrossRef]
52. Bhattacharjee, A.; Pilchak, A.; Lobkis, O.; Foltz, J.; Rokhlin, S.; Williams, J. Correlating Ultrasonic Attenuation and Microtexture in a Near-Alpha Titanium Alloy. *Metall. Mater. Trans. A* **2011**, *42*, 2358–2372. [CrossRef]
53. Zhang, C.; Li, X.; Song, Y.; Han, X.; Han, J. Evaluating the Grain Size in Curved Components Using the Ultrasonic Attenuation Method with Diffraction Correction. *NDT&E Int.* **2016**, *84*, 20–26. [CrossRef]
54. Bai, X.; Tie, B.; Schmitt, J.; Aubry, D. Comparison of Ultrasonic Attenuation within Two-and Three-Dimensional Polycrystalline Media. *Ultrasonics* **2020**, *100*, 105980. [CrossRef] [PubMed]
55. Aussel, J.; Monchalin, J. Precision Laser-Ultrasonic Velocity Measurement and Elastic Constant Determination. *Ultrasonics* **1989**, *27*, 165–177. [CrossRef]
56. Every, A.; Sachse, W. Determination of the Elastic Constants of Anisotropic Solids from Acoustic-Wave Group-Velocity Measurements. *Phys. Rev. B* **1990**, *42*, 8196. [CrossRef] [PubMed]
57. Lee, H.; Ando, S.; Coenen, J.; Mao, Y.; Riesch, J.; Gietl, H.; Kasada, R.; Hamaji, Y.; Ibano, K.; Ueda, Y. Longitudinal and Shear Wave Velocities in Pure Tungsten and Tungsten Fiber-Reinforced Tungsten Composites. *Phys. Scr.* **2017**, *T170*, 14024. [CrossRef]
58. Rose, J.L. *Ultrasonic Waves in Solid Media*; Cambridge University Press: Cambridgeshire, UK; pp. 24–30.